Geoscientific
Model Development

# Implementation of an intermediate-complexity snow-physics scheme (ISBA-Explicit Snow) into a sea ice model (SI³): 1D thermodynamic coupling and validation

Théo Brivoal[1], Virginie Guemas[1], Martin Vancoppenolle[2], Clément Rousset[2], and Bertrand Decharme[1]

[1]Centre National de Recherches Météorologiques (CNRM), Météo-France, CNRS, Université de Toulouse, Toulouse, France
[2]LOCEAN-IPSL, CNRS, Sorbonne Université, Paris, France

**Correspondence:** Théo Brivoal (theo.brivoal@meteo.fr)

**Abstract.** Snow plays a crucial role in the formation and sustainability of sea ice. Due to its thermal properties, snow acts as an insulating layer, shielding the ice from the air above. This insulation reduces the heat transfer between the sea ice and the atmosphere. Due to its reflective properties, the snow cover also strongly contributes to albedo over ice-covered regions, which gives it a significant role in the Earth's climate system.

Current state-of-art climate models use overly simple representations of the snow cover overlaying the sea ice. The snow cover is often represented with a one-layer scheme, assuming a constant density, no wet or dry metamorphism, or that no liquid water is stored in the snow. Here we implemented an intermediate-complexity snow-physics scheme (ISBA-Explicit Snow) into a sea ice model (SI³), which serves as the sea ice component for upcoming versions of the CNRM-CM climate model. This is, to our knowledge, the first time that a snow model with such a level of complexity has been incorporated into a sea ice model designed for global to regional applications. We validated our model by comparing 1D simulations with data from the Surface Heat Budget of the Arctic Ocean (SHEBA) but also simulations from another advanced snow-on-sea ice model (SnowModel-LG), as well as simulations with the previous SI³ snow scheme.

Our model simulates realistic snow thicknesses, densities, and temperatures, aligning well with SHEBA observations and SnowModel-LG outputs, while capturing their temporal variability. We show that the thickness, density, and thermal conductivity of the snowpack are significantly affected by the choices made in parameterization for calculating snowfall density and wind-induced snow compaction and by the choice of the atmospheric forcing. Unlike the previous SI³ snow scheme that assumed constant density and thermal conductivity, our model realistically simulates the evolution of these properties, resulting in more accurate temperatures at the snow–ice interface. Ultimately, our study shows that modeling the temporal changes in the density and thermal conductivity of the snow layers leads to more realistic upper sea ice temperatures and therefore to a more accurate representation of heat transfer between the underlying sea ice and the atmosphere.

## 1 Introduction

Snow is an important component of the climate system. Due to its reflective properties, it regulates the Earth's energy balance. Without snow, our planet would warm due to a positive feedback loop on the ocean, land, and atmosphere system (Webster et al., 2018). In the polar regions, snow accumulates on top of the sea ice, leading to an increase in the surface albedo by up to 50 % with respect to the bare ice albedo (e.g., Perovich and Polashenski, 2012) and to a reduction of the solar radiation absorbed by the sea ice (and thus the climate system). Conversely, snow on sea ice acts as an insulator (e.g., Sturm and Massom, 2017), reducing the heat transfer between the sea ice and the atmosphere and delaying the ice thermodynamic thickening, keeping the ice warm and thus thin (Fichefet et al., 2000; Lecomte et al., 2013). Snow

can also promote sea ice growth through the formation of superimposed ice (the refreezing of fresh percolating meltwater on top of sea ice; Nicolaus et al., 2003) and snow ice (refrozen mixture of snow and saltwater flooding the base of the snow; Jutras et al., 2016). Despite its importance, snow on sea ice remains an understudied component of the climate system.

The optical and thermal properties of snow are influenced by a multitude of processes that vary significantly in their frequency, magnitude, and occurrence across seasons, regions, and hemispheres (see Webster et al., 2018, and Sturm and Massom, 2017, for recent reviews). At microscopic scale, the freshly deposited snow undergoes complex metamorphic processes that modify its grain size, shape, and density, thus impacting its thermal conductivity (Sturm et al., 1997) and albedo (Bohren and Beschta, 1979). After snowfall, the wind erodes or drifts the unconsolidated snow, shaping the heterogeneity of the snow cover in accordance with the sea ice topography. Some of this blowing snow may also fall into leads, open cracks, or polynyas where it may melt, form slush, or refreeze (Leonard and Maksym, 2011). Wind also tends to compact the snowpack, thus increasing its density (Sommer et al., 2018).

Accurately representing snow on sea ice in climate models is crucial for capturing the complex interactions and feedbacks within the climate system and for ensuring more reliable predictions of future climate changes (Fichefet et al., 2000; Holland et al., 2021; Lecomte et al., 2013). For instance, Fichefet et al. (2000) showed that reducing by half the thermal conductivity of the snow overlaying the Antarctic sea ice in a global coarse-resolution ice–ocean model significantly decreases the sea ice thickness. They also observed changes in the stratification of the Southern Ocean and a weakening of the Antarctic Bottom Water meridional overturning. Similarly, in the Arctic, Lecomte et al. (2013) showed that using a constant snow conductivity in a coupled sea ice–ocean model leads to an overestimation of sea ice thickness in the Arctic. More recently, Holland et al. (2021) showed that increasing snow precipitation in climate models results in significant changes to sea ice thickness, emphasizing the critical need for an accurate representation of the snow cover on sea ice within coupled Earth system models.

While current state-of-the-art climate models employ relatively complex snow schemes over land, the scarcity of observations and the technical challenges involved in coupling snow with sea ice (Liston et al., 2020) lead to relying on overly simplistic representations of the snow on sea ice. Indeed, snow on sea ice in climate models is typically depicted using a simplified one-layer scheme, assuming constant snow density and thermal conductivity, without taking into account liquid water retention or snow metamorphism.

Over recent years, efforts have been made towards using more complex snow models over the sea ice. These models are mainly designed to produce datasets of snow properties such as (primarily) its thickness or (secondarily) density to compensate for the lack of observational data and/or assist with remote sensing (the snow thickness is a required input to derive the sea ice thickness from satellite altimetry). For example, Liston et al. (2020) developed for such applications a Lagrangian snow model (SnowModel-LG) which follows the ice motion and includes a representation of snow density and grain size evolution, blowing-snow sublimation, snowmelt, and superimposed ice formation. Similarly, Wever et al. (2020) developed a sea ice module for the unidimensional, physics-based, detailed, multi-layer snow cover model SNOWPACK, which they used in a Lagrangian framework.

Such Lagrangian models are useful to improve the knowledge of the interactions between snow and sea ice but are not suitable for climate systems that use an Eulerian framework. Simple modeling of snow on sea ice with an Eulerian framework has also been achieved. Lecomte et al. (2013) developed a parameterization that consists of a set of two linear equations relating the snow thermal conductivity and density to the mean seasonal wind speed. More recently, Petty et al. (2018) developed an Eulerian model which uses two snow layers, a rather simple parameterization representing accumulation, wind packing, advection–divergence, and blowing snow lost to leads to represent key sources and sinks of snow on sea ice. In the CICE sea ice model (Hunke et al., 2017), snow physics are handled by the Icepack component (Shapero et al., 2021), which includes some advanced parameterizations such as wind-driven snow erosion and compaction. In this scheme, an effective snow density is diagnosed based on wind speed and used to limit erosion of denser snow layers. Additionally, the model parameterizes the snow grain size evolution as a function of temperature gradients and density, which in turn influences surface albedo.

The sea ice component for upcoming versions of the CNRM climate model (CNRM-CM, Voldoire et al., 2013), called SI$^3$ (Sea Ice modeling Integrated Initiative, Vancoppenolle et al., 2023), incorporates a simplistic representation of snow over sea ice, assuming a constant density, thermal conductivity, and albedo. In this study, we integrate a more advanced snow scheme, ISBA-Explicit Snow, (ISBA-ES, Boone and Etchevers, 2001), into SI$^3$ to improve its representation of the snow over sea ice. The ISBA-ES snow model incorporates detailed representations of snowpack properties such as density, grain size, and thermal conductivity, allowing for more accurate simulation of snow accumulation, compaction, metamorphism, and melt processes than previous snow schemes within SI$^3$. To the best of our knowledge, this is the first time a snow-physics scheme of this level of complexity has been integrated into a global sea ice model.

Here, we present the SI$^3$ + ISBA-ES model, the developments made to allow the integration of ISBA-ES within the SI$^3$ framework, and the validation of our coupled model in a unidimensional context focusing on the thermodynamic processes only (i.e., without representing the effects of sea ice dynamics). To achieve this, we decided to validate our model

using Lagrangian data from the Surface Heat Budget of the Arctic Ocean (SHEBA) experiment (Perovich et al., 1999), where there are no direct effects of sea ice drift on snow properties, and against SnowModel-LG (Stroeve et al., 2020) data.

## 2 Materials and method

### 2.1 Sea ice model

The sea ice model used is SI$^3$ (Sea Ice modeling Integrated Initiative, Vancoppenolle et al., 2023), which is part of the Nucleus for European Modelling of the Ocean (Madec and the NEMO System Team, 2024) in its version 4.2.2. The core of SI$^3$ integrates a suite of physical processes crucial for accurately simulating sea ice evolution. These processes include thermodynamics, where heat exchanges between the atmosphere, ocean, and ice drive ice growth and melt. Additionally, SI$^3$ accounts for mechanical forces such as ice deformation and ridging, which significantly impact ice thickness distribution and overall sea ice morphology. The sea ice thermodynamics are modeled using a 1D scheme that conserves energy (Bitz and Lipscomb, 1999) and includes a time-dependent salinity profile (Vancoppenolle et al., 2009). SI$^3$ resolves a subgrid-scale sea ice thickness distribution (Bitz et al., 2001; Thorndike et al., 1975). As the paper focuses on thermodynamics, we use the SI$^3$ model in 1D (vertical) configurations, with only one sea ice category and two ice layers, assuming that the dynamical processes affecting the snow and sea ice such as the ice deformation and ridging are negligible and that the advection is accounted by following the trajectory of the observations used to validate the model (see Sect. 2.4). Since we focus on the period where the snow is present, we neglect melt ponds over sea ice in our configurations.

The surface forcing is computed by the NEMO bulk algorithm (NCAR; Large and Yeager, 2004). Turbulent heat fluxes over sea ice are computed from 2 m air temperature and humidity, 10 m winds, and surface pressure. In the current version of the model, the snow fraction is either 1 or 0, meaning that we assume that the snow covers the whole ice fraction.

### 2.2 Snow model

The original version of the SI$^3$ model used for this paper, prior to any snow model implementation, simulates the snow cover assuming constant density (330 kg m$^{-3}$) and thermal conductivity (0.31 W m$^{-1}$ K$^{-1}$), no liquid water stored in snow, and no snow metamorphism. When SI$^3$ is hereafter coupled with the ISBA-ES snow model (see Sect. 2), the snow cover is simply computed by ISBA-ES instead of the original SI$^3$ trivial snow scheme.

The ISBA-Explicit Snow (ISBA-ES) snow model (Interactions between Soil Biosphere Atmosphere-Explicit Snow)

was developed by Boone and Etchevers (2001) and revised by Decharme et al. (2016) (see also the user manual, Boone, 2002). Initially developed for alpine conditions, it incorporates detailed representations of snowpack properties such as density, grain size, and thermal conductivity and accounts for complex processes like snow accumulation, compaction, dry and wet metamorphism, liquid water storage, and melt processes. The model is based on similar schemes as described by Kondo and Yamazaki (1990), Loth et al. (1993), Lynch-Stieglitz (1994), and Sun et al. (1999). We use 12 snow layers for our simulations. The number of vertical layers is fixed but their thickness is adapted at each time step to the total snow thickness, and the ISBA-ES prognostic variables are remapped at each time step on the ISBA-ES vertical grid. At each time step, the snow layer thickness is updated according to the total snow thickness. The upper layer thickness is bounded so that its thickness does not exceed 0.2 m in order to resolve the diurnal cycle based on an assumed thermal damping depth of snow (Boone and Etchevers, 2001). Thickening beyond that threshold ultimately results in snow transfer toward the layers below. The prognostic variables of the model are the snow heat content, the snow density, the snow thickness, and the snow albedo. ISBA-ES includes parameterizations for processes like snow sublimation, blowing-snow transport, and snowfall density, enabling a comprehensive understanding of the physical mechanisms driving the snowpack evolution. The snow metamorphism is not explicitly computed but is accounted for in the density and albedo parameterizations.

### 2.2.1 Snow density

The local rate of change of snow density $\rho_s$ is parameterized after Brun et al. (1989, 1997):

$$\frac{\partial \rho_s}{\partial t} = \frac{\sigma_s}{\eta_s(T_s, \rho_s)} + \xi_{\text{wind}}. \tag{1}$$

The first term on the right-hand side represents the snow overburden (the compactive viscosity term). It accounts for the pressure of the snow above ($\sigma_s$, in Pa) and its viscosity ($\eta_s$, in Pa s), determined by snow temperature $T_s$ and density $\rho_s$ (Kojima, 1967; Mellor, 1964). The second, term $\xi_{\text{wind}}$, represents the effect of the wind compaction (see Sect. 2.2.3).

### 2.2.2 Energy balance and heat flow

The heat content $H_s$ (in J m$^{-2}$) or energy needed to melt each snow layer is defined using an expression similar to those of Lynch-Stieglitz (1994) and Sun et al. (1999) as

$$H_s = c_s h_s (T_s - T_f) - L_f (W_s - W_l), \tag{2}$$

where $h_s$ is the snow thickness, $L_f$ is the latent heat of fusion, $c_s$ is the snow heat capacity defined following Verseghy (1991), $W_s$ is the snow water equivalent (SWE), and $W_l$ is the

snow liquid water content. The heat content is used to diagnose the snow temperature using the equation above assuming that there is no liquid water in the snow layer ($W_l = 0$).

$$T_s = T_f + \frac{H_s + L_f W_s}{c_s h_s} \tag{3}$$

If the calculated temperature exceeds the freezing point, it is set to $T_f$, and the liquid water content is determined from the heat content equation as follows:

$$W_l = W_s + \frac{H_s}{L_f}. \tag{4}$$

The layer-averaged snow temperature equation ($T_{s,k}$) for the snow layer $k$ is then expressed as

$$c_{s,k} D_{s,k} \frac{\partial T_{s,k}}{\partial t} = G_{s,k-1} - G_{s,k} - F_{s,k}, \tag{5}$$

where $F_s$ represents latent heat absorption or release due to phase changes (between water and ice). The heat flux $G_s$ is simply expressed as

$$G_s = J_s + Q_s, \tag{6}$$

where $J_s$ and $Q_s$ are the heat conduction and radiation fluxes, respectively. $Q_s$ is computed as follows:

$$Q_{s,i} = R_g (1 - \alpha) \exp(-\nu_{s,k} h_{s,k}) k_s, \tag{7}$$

where $R_g$ is the incoming shortwave radiation at the snow surface, $\alpha$ is the albedo, and $\nu_{s,k}$ is the shortwave radiation extinction coefficient (Bohren and Barkstrom, 1974). The extinction coefficient $\gamma_{s,i}$ at each snow level $i$ is computed as in Anderson (1976) and depends on the snow optical diameter $d_{s,i}$ such as $\gamma_{s,i} = C_v \rho_{s,i} d_{s,i}^{-1/2}$. The snow optical diameter is itself parameterized after Anderson (1976) and depends on the snow density as $d_{s,i} = \mathrm{MIN}(d_{s,max}, a_{sd} b_{sd} \rho_{si}^4)$, where $d_{s,max}$ is the maximum grain size authorized and is equal to $2.796 \times 10^{-3}$ m. The snow albedo is solved over three bands (ultraviolet and visible, 0.3–0.8 μm; two near-infrared bands, 0.8–1.5 μm and 1.5–2.8) as in Decharme et al. (2016, Eq. 17) and is a function of the snow optical diameter and of the age of the first layer of the snowpack. The conduction flux $J_s$ is computed as follows:

$$J_{s,i} = \frac{2 k_{s,k}(T_{s,k} - T_{s,k+1})}{h_{s,k} + h_{s,k+1}}, \tag{8}$$

where $h_{s,k}$ is the snow layer thickness, and $k_s$ is the snow thermal conductivity. Finally, the net heat flux $G_{s,0}$ at the atmosphere–snow interface is expressed as

$$\begin{aligned} G_{s,0} = R_g(1 - \alpha) + \varepsilon_n R_{at} - \sigma T_{s,1}^4 - H - \mathrm{LE} \\ + P_{rn} C_w (T_{al} - T_f), \end{aligned} \tag{9}$$

where $\varepsilon_n$ is the snow emissivity (assumed to be 1), $R_{at}$ is the downwelling atmospheric longwave radiation, $\sigma$ is the

Stefan–Boltzmann constant, and $H$ and LE are the sensible and latent heat fluxes. The last term on the right-hand side of the equation above is a precipitation advection term where $c_w$ represents the specific heat of water, $P_{rn}$ is the rainfall rate, and $T_{al}$ is the temperature of rainfall, assumed to be the air temperature if it is above the temperature of fusion $T_f$.

### 2.2.3 Parameterizations

ISBA-ES uses parameterizations to represent various processes, including the changes in snow albedo, grain size, radiation extinction coefficient, compactive viscosity (that represent the snow overburden), thermal conductivity, snowfall density, and snow compaction due to wind (see Sects. 2.2.1 and 2.2.2). For the purposes of this study, some of the parameterizations were adjusted to better suit polar conditions. Thus, this section only outlines the parameterizations that differ from the standard ISBA-ES configuration as described by Decharme et al. (2016). Detailed descriptions of the parameterizations that remained unchanged from the default ISBA-ES configuration for this study are available in Boone and Etchevers (2001) and Decharme et al. (2016).

#### Snowfall density

The density of the snow precipitation is parameterized as in Pahaut (1975):

$$\rho_{new} = A_{sn} + B_{sn}(T_a - T_f) + C_{sn}(V_a)^{1/2}, \tag{10}$$

where $T_a$ is the air temperature, $T_f$ is the temperature of fusion, and $V_a$ is the 10 m wind speed. $A_{sn}$, $B_{sn}$, and $C_{sn}$ are coefficients given by Pahaut (1975). Additionally, we tested another set of values for these coefficients, supposedly more suitable to the Arctic region given by Royer et al. (2021). The values of the coefficients are listed in Table 1.

#### Wind compaction

The snowpack density is increased by the wind compaction processes. In ISBA-ES, the snowdrift $\xi_{wind}$ (i.e., the wind compaction) is computed as

$$\xi_{wind} = \frac{\partial \rho_{s,k}}{\partial t} = \frac{\rho_{max} - \rho_{s,k}}{\tau_i}, \tag{11}$$

where $k$ denotes the snow layer, $\rho_{max}$ is a maximum snow density authorized, and $\tau_i$ is the time characteristic for snow grain change under wind transport and is computed as

$$\tau_k = \frac{\tau}{\mathrm{Wind}_{Effect} \Gamma_{k,drift}}, \tag{12}$$

where $\tau$ is empirically set to 48 h, $\mathrm{Wind}_{Effect}$ is an empirical coefficient on wind effect, and $\Gamma_{k,drift}$ represents the grain driftability with an exponential decay function of the depth of the snow layer. In our experiments, we use two sets of values for the parameters $\rho_{max}$ and $\mathrm{Wind}_{Effect}$. The first one is the

**Table 1.** Coefficients used for the parameterization of the snowfall density.

| Coefficient | $A_{sn}$ $(\mathrm{kg\,m^{-3}})$ | $B_{sn}$ $(\mathrm{m^{-3}\,K^{-1}})$ | $C_{sn}$ $(\mathrm{m^{-7/2}\,s^{1/2}})$ | $\rho_{max}$ (for wind compaction) |
|---|---|---|---|---|
| Pahaut (1975) | 109 | 6 | 26 | 350 |
| Royer et al. (2021) | 109 | 6 | 59 | 600 |

default parameters used in ISBA-ES, defined by Brun et al. (1997), where $\rho_{max} = 350\,\mathrm{g\,m^{-3}}$ and $\mathrm{Wind_{Effect}} = 1$, and the second one is the parameters defined by Royer et al. (2021), where $\rho_{max} = 600\,\mathrm{g\,m^{-3}}$ and $\mathrm{Wind_{Effect}} = 1.5$, in order to increase the effect of the wind on compaction and improve the representation of the upper wind slab layer typical of Arctic snowpacks (e.g., Domine et al., 2018; Sturm et al., 2002, and references therein).

**Thermal conductivity**

In the default version of ISBA-ES, the thermal conductivity is computed as in Anderson (1976). However, this parameterization may not be suited to the Arctic region. For this reason, and to be consistent with the SnowModel-LG model used for comparison and validation (Liston et al., 2020, and see Sect. 2.4), we implemented the Sturm et al. (1997) parameterization for the thermal conductivity, which is computed as follows:

$$k_s = 0.138 - 1.01\rho + 3.233\rho^2 \quad 0.156 \leq \rho \leq 0.6 \tag{13a}$$

and

$$k_s = 0.023 + 0.234\rho \quad \rho \leq 0.156. \tag{13b}$$

**2.3   Snow and ice coupling**

In this work, we couple the ISBA-ES model to the SI$^3$ model so that most snow thermodynamic processes are not computed anymore by the original SI$^3$ snow scheme but by ISBA-ES. However, some sea-ice-related processes (not accounted for in the ISBA-ES original model) such as the snow–ice formation are not resolved by the current version of ISBA-ES and are still resolved within the sea ice model. The coupling is made online, meaning that the ISBA-ES code is incorporated within SI$^3$ and no coupler is needed. However, in the present version of the code the interactions of the snow with the sea ice dynamics and with the melt ponds are not yet implemented so we focus on evaluating the thermodynamic part of the coupling.

At the beginning of a time step, the lower boundary condition of ISBA-ES is given by the temperature and the thermal conductivity of the upper sea ice layer. After the resolution of snow processes, the conduction flux at the snow–ice interface computed by ISBA-ES is sent to SI$^3$ and is used as upper boundary condition for the temperature solving in

the sea ice. Note that since the snow–ice conversion is computed within SI$^3$ and not ISBA-ES, the vertical profiles of the ISBA-ES prognostic variables are also exchanged between the two models and updated in both ISBA-ES (due to "snow-only" processes) and SI$^3$ (due to snow–ice conversion).

The conduction flux at the snow–ice interface $F_c$ is recomputed in ISBA-ES as $F_c = -K_{s-i} \cdot (T_{i,1} - T_{s,N})$, where $T$ is the temperature, the subscripts $i$ and $s, N$ denote the ice or the snow and the index 1, and $N$ denotes the upper layer and the lower layer, respectively. $K_{s-i}$ is the thermal conductivity at the snow–ice interface, which is computed as in SI$^3$ and Rousset et al. (2015): $K_{s-i} = \frac{(h_{s,N}+h_{i,0}) \cdot (k_{i,0} \cdot k_{s,N})}{(k_{i,0} \cdot h_{s,N} + k_s \cdot h_{i,0})}$, where $k$ is the thermal conductivity and $h$ is the thickness of the corresponding layer (depending on the subscript).

The ISBA-ES model is called just before the resolution of the sea ice thermodynamic processes. The basic iteration procedure for the SI$^3$ + ISBA-ES model follows the steps below.

- The ISBA-ES model is called. The model reads its prognostic variables (snow thickness, density, heat content, and albedo) from a restart or from a previous time step and the temperature and conductivity of the first sea ice layer from current time step. Then, it computes the changes in snow thickness, heat content, and density due to snowfall and remaps the prognostic variables on its vertical grid. Then, the model resolves the evolution of prognostic variables accounting for processes such as settling, compaction, metamorphism, and melting. Additionally, it calculates the conduction flux at the interface between the snow and sea ice and the radiative flux transferred to the sea ice below. At the end of the ISBA-ES iteration, the vertical profiles of ISBA-ES prognostic variables along with any remaining heat and evaporation flux to be transmitted to SI$^3$ (if all snow has melted during a time step) are stored.

- The conduction flux at the interface between the snow and the sea ice estimated by ISBA-ES is then used as a boundary condition to solve the temperature equation in the sea ice by SI$^3$, and changes in ice thickness due to ice melt are computed by SI$^3$ as well.

- If the snow exceeds a certain thickness and density so that the snow base is pushed below the freeboard, snow–ice formation occurs, and the vertical profiles of

snow and sea ice thickness and enthalpy are updated and saved for use in the next time step.

Note that the current version of the $SI^3$ + ISBA-ES model does not yet account for the dynamic processes related to the sea ice advection and deformation and thus cannot be used to perform realistic 3D simulations. Nonetheless, the version of the model presented here is already suitable for 1D simulations on multiyear ice, following the ice motion.

## 2.4  Validation data

We use the data collected during the Surface Heat Budget of the Arctic Ocean (SHEBA) experiment to validate our model (Perovich et al., 1999). The SHEBA experiment took place from 1997 to 1998. During this period, several snow variables useful to validate our model such as the snow thickness, the snow surface temperature, and the snow–ice interface temperature were collected daily. Snow thicknesses were gathered by employing magnaprobes and ruler measurements along transects ranging from 200 to 500 m in length. We used the same SHEBA snow thickness dataset as Stroeve et al. (2020), where in situ observations were aggregated over all transects and averaged for each day. Since most snow measurement were taken on multiyear ice (Sturm et al., 2002), the snow depth averaged over all transects can be approximated as the snow depth on level ice. Additionally, the snow surface temperature and the snow–ice interface temperature were collected from thermistors as described in Persson et al. (2002). Note that the two temperatures were not measured exactly at the same exact location, leading to an uncertainty of $\sim 0.6\,°C$ in the temperatures.

We also compared our model with the outputs of the SnowModel-LG simulations performed by Liston et al. (2020) and Stroeve et al. (2020). SnowModel-LG is a multilayer model specifically designed to simulate the key physical processes governing the seasonal evolution of snow thickness and density over sea ice. It operates on a Lagrangian framework and incorporates various parameterizations to account for processes like blowing-snow redistribution, sublimation, changes in density and grain size, and snow metamorphism. More details about the model can be found in by Liston et al. (2020) and Stroeve et al. (2020). The model is forced either by NASA's Modern Era Retrospective Analysis for Research and Applications Version 2 (MERRA-2, Gelaro et al., 2017) or by the European Centre for Medium-Range Weather Forecasts (ECMWF) atmospheric data (ERA5, Hersbach et al., 2020). Approximately 61 000 Lagrangian parcels were simulated with this model over the Arctic, covering the 1980–2018 period. We also use the SnowModel-LG data described in Stroeve et al. (2020), which gives an estimate of the classic behavior of a snow model of intermediate complexity. To compare SnowModel-LG with our simulations over the SHEBA site, we used the same Lagrangian parcel used in Stroeve et al. (2020), which is a representative parcel located initially near the departure
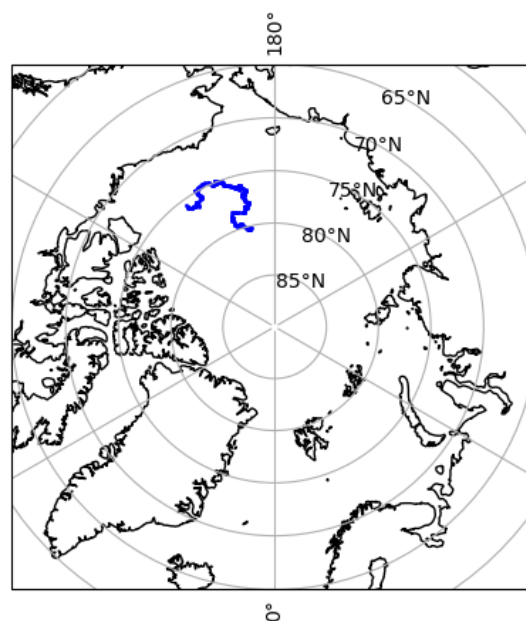


**Figure 1.** Trajectory of the SHEBA experiment during the observation period (blue).

location of the SHEBA campaign (see Sect. 3.1 in their paper). The path of the SHEBA experiment is illustrated in Fig. 1.

More recent campaigns than SHEBA have measured snow over sea ice over nearly year-long periods, notably the MOSAiC campaign (Nicolaus et al., 2022). However, cumulative snowfall during MOSAiC showed significant variability across transects – up to 10 times higher than the mean in some cases – due to intense blowing-snow events (Wagner et al., 2022). In contrast, SHEBA reported only a 30 % increase in snow depth over ridges (Sturm et al., 2002). Additionally, the average cumulative snowfall across all MOSAiC transects was relatively low, ranging from 72 to 107 mm SWE, with a peak snow depth of 30 cm (Itkin et al., 2023). This contrasts with the SHEBA campaign, where cumulative snowfall reached around 179 mm SWE and snow depth peaked at 42.3 cm, with an average of 37.3 cm (Sturm et al., 2002). For these reasons, we chose to use the SHEBA dataset instead of MOSAiC to validate our model.

## 2.5  Configurations

Among all the parameterizations available in ISBA-ES, the parameterizations of the snowfall density and of the wind-induced compaction are the ones with the greatest impact on the snow thickness and density. Thus, we performed a set of experiments to evaluate the sensitivity of the model to these parameterizations. Two experiments, P76 and R21 using the Pahaut (1975) and Royer et al. (2021) coefficients (see Sect. 2.2.3) for the parameterization for the snowfall density, respectively, were conducted without the snow-

**Table 2.** Parameterizations used to represent snow processes in all $SI^3$ + ISBA-ES (and $SI^3$-only) simulations.

| Simulation name | Configuration | Snow compaction (due to overburden) | Snowfall density | Thermal conductivity | Metamorphism | Snowdrift (compaction by wind) | Albedo |
|---|---|---|---|---|---|---|---|
| $SI^3$ | $SI^3$ | Constant, $330\,\mathrm{kg\,m^{-3}}$ | Constant, $330\,\mathrm{kg\,m^{-3}}$ | Constant, $0.31\,(\mathrm{W\,m^{-1}\,K^{-1}})$ | None | None | Constant, 0.83 |
| P76 | $SI^3$ + ISBA-ES | Brun et al. (1989) and Vionnet et al. (2012) | Pahaut (1975) | Sturm et al. (2002) | Parameterized in density and albedo formulations | None | Douville et al. (1995) |
| P76_DRIFT | $SI^3$ + ISBA-ES | Brun et al. (1989) and Vionnet et al. (2012) | Pahaut (1975) | Sturm et al. (2002) | Parameterized in density and albedo formulations | Brun et al. (1997) | Douville et al. (1995) |
| R21 | $SI^3$ + ISBA-ES | Brun et al. (1989) and Vionnet et al. (2012) | Royer et al. (2021) | Sturm et al. (2002) | Parameterized in density and albedo formulations | None | Douville et al. (1995) |
| R21_DRIFT | $SI^3$ + ISBA-ES | Brun et al. (1989) and Vionnet et al. (2012) | Royer et al. (2021) | Sturm et al. (2002) | Parameterized in density and albedo formulations | Brun et al. (1997) | Douville et al. (1995) |
| R21_DRIFT21 | $SI^3$ + ISBA-ES | Brun et al. (1989) and Vionnet et al. (2012) | Royer et al. (2021) | Sturm et al. (2002) | Parameterized in density and albedo formulations | Royer et al. (2021) | Douville et al. (1995) |

drift parameterizations active. Additionally, two similar experiments, P76_DRIFT and R21_DRIFT, were conducted with the snowdrift parameterization enabled, using the Pahaut (1975) and Royer et al. (2021) coefficients, respectively, for snowfall density parameterization. Another experiment, named R21_DRIFT21, was set up using the Royer et al. (2021) coefficients for both snowfall density and snowdrift parameterization (see Sect. 2.2.3). Lastly, we prepared a configuration called $SI^3$, where the snowpack is simulated by $SI^3$ in its NEMO 4.2 stable version (i.e., without ISBA-ES) to examine the differences in snow state simulation between $SI^3$-only and $SI^3$ + ISBA-ES. The parameterizations used in these experiments are summarized in Table 2.

$SI^3$ is used in sea-ice-only mode, meaning that the sea ice and snow component is forced from both oceanic and atmospheric sides. We use the GLORYS12 (Lellouche et al., 2018) reanalysis as forcing data for the ocean and either the MERRA-2 or ERA5 reanalysis for the atmosphere (more information is provided in the Results section). To force our simulations, we followed the trajectory of the SHEBA tower and extracted the forcing data at the position of the tower for each day.

The simulations were initialized on 3 November 1997. We use the SHEBA snow thickness averaged over all snow transects for this date (0.153 m) as the initial value for our model. We also use the SnowModel-LG density for this date ($191\,\mathrm{kg\,m^{-3}}$) to initialize ISBA-ES simulations since the density for SHEBA was not measured on this date. For the sea ice thickness and concentration, we use the GLORYS12 value for this date (2.95 m and 0.88, respectively).

## 3   Results

### 3.1   Validation at the SHEBA site

#### 3.1.1   Sensitivity to the atmospheric forcing

Following Stroeve et al. (2020), we first investigate the effect of the atmospheric forcing on the snowpack variability. For this, we conducted two simulations using the P76_DRIFT setup, changing only the atmospheric forcing applied – either ERA5 or MERRA-2 – over the duration of the SHEBA experiment (Perovich et al., 1999), following the tower trajectory. We compare the results obtained from our simulations with the SHEBA data and with the outputs available from the SnowModel-LG simulations from Liston et al. (2020) and Stroeve et al. (2020). While the resolution disparity between our model's estimates (roughly equivalent to the resolution of the forcing, 31 km for ERA5) and the point measurements from SHEBA prevents a quantitative assessment of our simulations, it does provide an estimate of the simulation's realism.

Overall, the snow thickness computed by ISBA-ES with the P76_DRIFT configuration compares well with the SHEBA observations and SnowModel-LG outputs (Fig. 2). When using ERA5 as the atmospheric forcing, snow thickness is slightly underestimated by an average of 3.4 cm over the period. In contrast, a better match with observations is achieved using MERRA-2, with the underestimation reduced to an average of 0.5 cm (refer to the scores in Table 3). In particular, the snowmelt is delayed in comparison to the ERA5 simulation because MERRA-2 reports more precipitation than ERA5 during the melt season (from May to August). During the SHEBA period, switching the atmospheric forc-
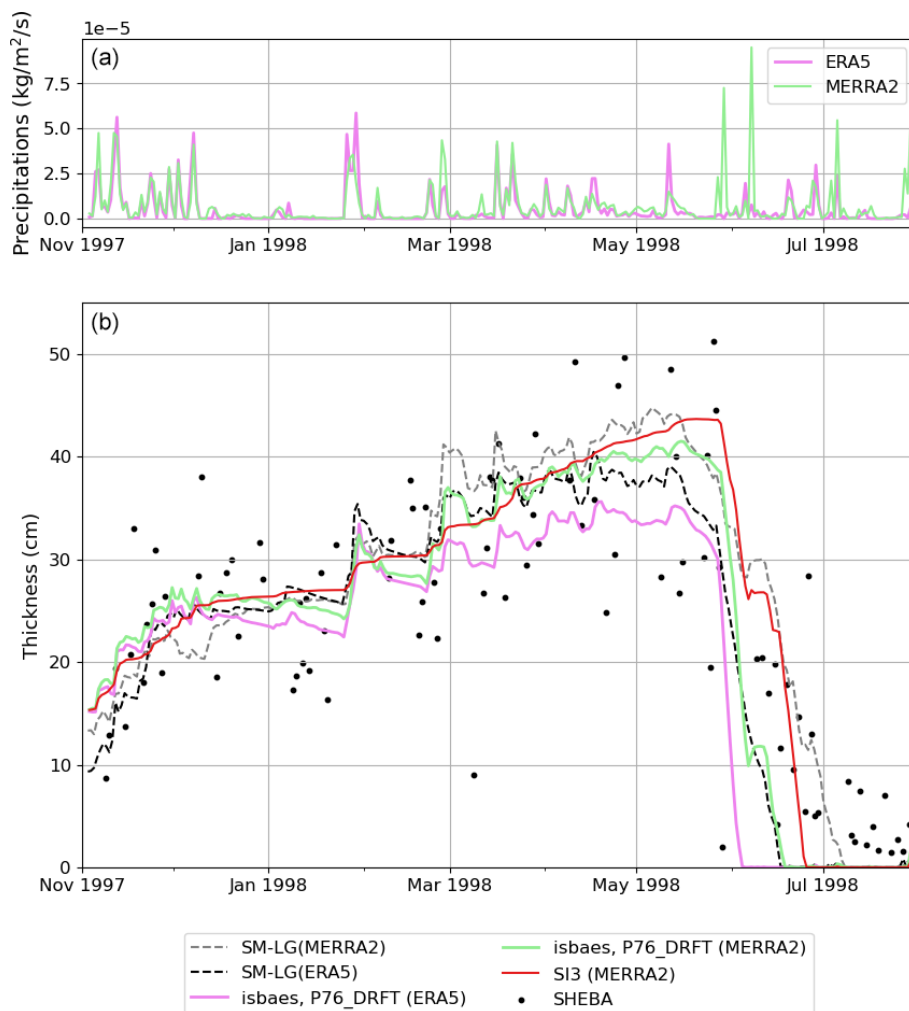
**Figure 2. (a)** Snow precipitation (in $kg\,m^{-3}\,s^{-1}$) in MERRA-2 (green line) and ERA5 (magenta line) forcings. **(b)** Observed daily averages (black dots) and simulated (lines) snow thickness at the SHEBA tower during the November 1997–September 1998 period. The observations were aggregated over all transects (Perovich et al. 1999). The magenta line and the green line represent the snow thickness for a simulation using the P76_DRIFT configuration using ERA5 and MERRA-2 as forcing, respectively. The dashed lines represent the snow thickness from the SnowModel-LG product, in light gray for the MERRA-2 forcing and dark gray for ERA5.

**Table 3.** Averaged scores obtained for the snow thickness (cm) during the November 1997 to August 1998 period for the sensitivity tests on the atmospheric forcing.

| Simulation | Mean (cm) | Mean difference with observations (cm) | Mean RMSE with observations (cm) | $R^2$ (with observations) |
|---|---|---|---|---|
| P76_DRIFT (ERA5) | 21.7 | −3.4 | 7.0 | 0.79 |
| P76_DRIFT (MERRA-2) | 24.9 | −0.5 | 6.7 | 0.79 |
| $SI^3$ (MERRA-2) | 26.4 | 1.4 | 6.7 | 0.78 |

ing from ERA5 to MERRA-2 results in an average change in snow thickness of approximately 3.2 cm in ISBA-ES simulations. This difference aligns with SnowModel-LG outputs, where the change in atmospheric forcing leads to an average change in snow thickness of around 3.1 cm.

The mean differences of P76_DRIFT simulations with SnowModel-LG outputs are 2.2 cm for ERA5 simulations and 2.1 cm for MERRA-2. The temporal variability of $SI^3$ + ISBA-ES simulations aligns more closely with the SnowModel-LG outputs compared to the $SI^3$-only simulation, where the snow thickness varies less over time. This is
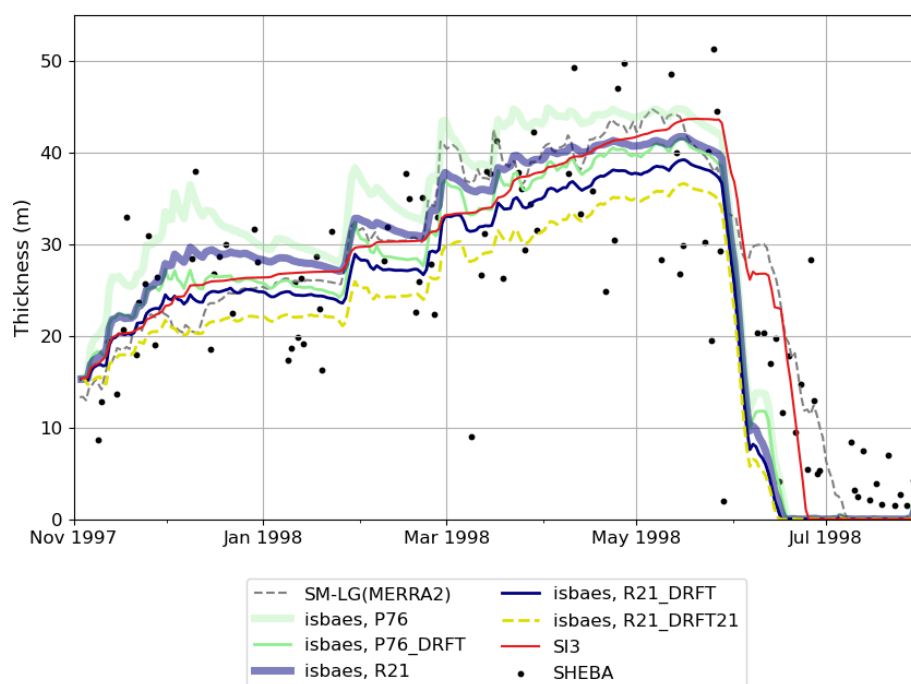
**Figure 3.** Observed daily averages (black dots) and simulated (lines) snow thickness at the SHEBA tower during the November 1997–September 1998 period. The observations were aggregated over all transects (Perovich et al. 1999). The thick green, thin green, thick blue, thin blue, yellow dashed, and red lines respectively show the P76, P76_DRFT, R21, R21_DRFT, R21_DRFT21, and SI$^3$-only simulations, while the dashed gray line shows the SnowModel-LG data.

because SI$^3$ + ISBA-ES simulates the temporal evolution of precipitation density, making it more responsive to changes in atmospheric temperature and wind compared to the SI$^3$-only simulation in which the density of the snowfall is constant.

### 3.1.2 Sensitivity to the parameterization of snowfall density and snowdrift

This section focuses on analyzing the effects of changing the parameterizations for snowfall density and wind-driven snow compaction (snowdrift). Given that better agreement with the observations was achieved using MERRA-2 as atmospheric forcing, we decided to use this forcing for our simulations. Therefore, the MERRA-2 reanalysis is used to force all simulations presented in the rest of the article.

We performed six simulations with the P76, P76_DRFT, R21, R21_DRFT, R21_DRFT21, and SI$^3$ configurations over the period and the path of the SHEBA experiment (Perovich et al., 1999) as described in the previous section.

Figure 3 depicts the aggregated snow thickness from all SHEBA transects compared to our simulations and to SnowModel-LG outputs. The scores obtained for each simulation are summarized in Table 4. Overall, all simulations compare reasonably well with the measured snow thickness from SHEBA during the accumulation period. The best scores are nonetheless obtained for the P76_DRFT simula-

tion (see Table 4). As expected, the snowdrift parameterization tends to reduce the snow thickness through snow compaction by $\sim 3.9$ cm (P76 – P76_DRIFT) on average over the period for the default parameters and by $\sim 5.1$ cm with the Royer et al. (2021) parameters for the snowdrift and the snowfall density (R21 – R21_DRIFT21). The choice of the parameterization for the snowfall density and for the snowdrift results in an average change in snow thickness of approximately 3.9 cm in ISBA-ES simulations (P76_DRIFT – R21_DRIFT21), which is roughly the same order of magnitude as the thickness change associated with the choice of atmospheric forcing (see Sect. 3.1.1).

However, the snow tends to disappear in all simulations during the first month of the melting season, while it persists until the end of the melting season (roughly from May to August) in the observations. In the melt season (from May 1998), the excessively fast melting of the snow in all ISBA-ES simulations compared to the SHEBA observations and the SI$^3$-only simulation is likely due to the ISBA-ES albedo parameterization, which seems to underestimate the albedo during the melt season. Indeed, when the snow albedo is forced to 0.8 (which is higher than the albedo simulated with ISBA-ES, see Fig. 9), the snow thickness gets closer to the SnowModel-LG simulation during the melt period (see Fig. S1 in the Supplement). This underestimation of the albedo is probably due to its dependency on the density. Indeed, the albedo depends on the snow specific area, which is

**Table 4.** Averaged scores obtained for the snow thickness (cm) during the November 1997 to August 1998 period for the sensitivity tests on the snow density parameterizations.

| Simulation | Mean (cm) | Mean difference with observations (cm) | Mean RMSE with observations (cm) | $R^2$ (with observations) |
|---|---|---|---|---|
| P76 | 28.8 | 3.1 | 8.0 | 0.78 |
| P76_DRIFT | 24.9 | −0.5 | 6.7 | 0.79 |
| R21 | 26.0 | 0.6 | 7.1 | 0.79 |
| R21_DRIFT | 23.2 | −2.0 | 6.9 | 0.79 |
| R21_DRIFT21 | 20.9 | −4.0 | 7.3 | 0.78 |
| SI$^3$ | 26.4 | 1.4 | 6.7 | 0.78 |
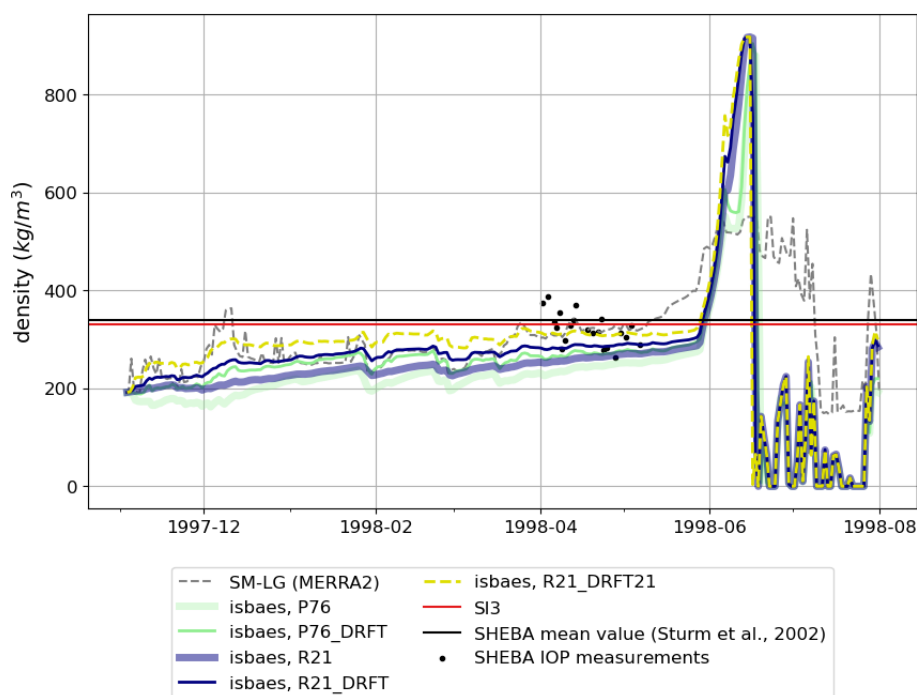


**Figure 4.** Snow density at the SHEBA tower during the November 1997–September 1998 period. The black dots represent the daily averages of the SHEBA density measurements made during the intensive observation period in April.

affected by the snow metamorphism (which is not explicitly represented by ISBA-ES), rather than on the snow density (e.g., Xiong and Shi, 2018)

The SI$^3$-only simulation reproduces the snowmelt more successfully, resulting in thicker snow during this period. The better performance of the SI$^3$-only simulation during the melt season may be attributed to its use of a constant snow albedo (0.83, see Fig. 9).

Note that the snow melts completely in summer in all simulations (including SnowModel-LG simulations), whereas snow remains in the observations, which also shows that the snowmelt is likely to be overestimated by the models.

The first-order discrepancies in snow thickness between the different ISBA-ES simulations are related to the density of snow: since during compaction processes the mass remains constant, a denser snow will be associated with a

thinner snowpack and vice versa. The evolution of the density during the SHEBA period is represented in Fig. 4. For the ISBA-ES simulations, the mean densities over this period are 225.6, 260.7, 244.6, 275.5, and 303.9 g m$^{-3}$ for P76, P76_DRIFT, R21, R21_DRIFT, and R21_DRIFT21, respectively, which is slightly lower than the average bulk density of 340 g m$^{-3}$ measured during SHEBA by Sturm et al. (2002) and with the mean densities of SnowModel_LG outputs (281.8 g m$^{-3}$ when forced by MERRA-2 and 263.0 when forced by ERA5). Better agreement with the SnowModel-LG depth-averaged density is found for the ISBA-ES simulations using the snowdrift parameterization (P76_DRIFT and R21_DRIFT).

Over the Arctic region, the snowpack typically consists of a basal depth hoar (low-density, brittle, highly permeable type of snow) overlaid by a hard and dense wind slab
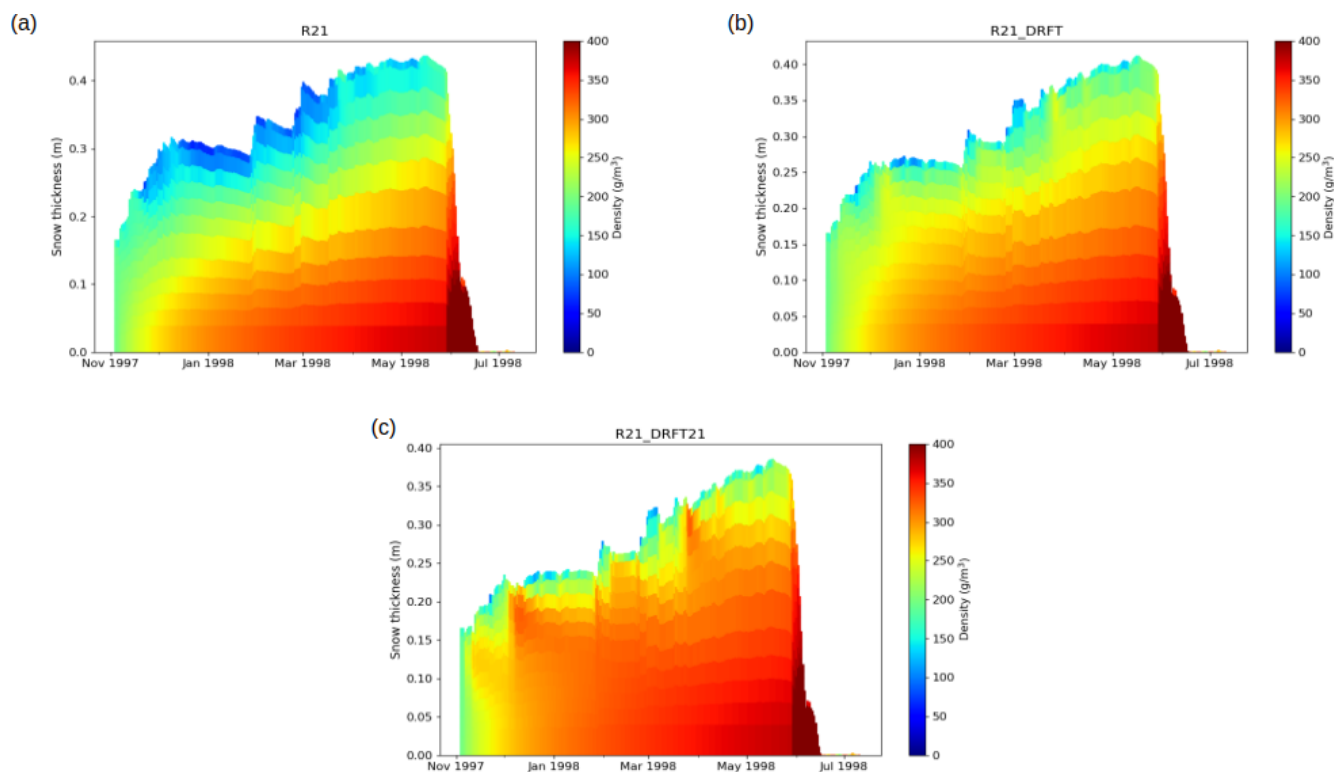
**Figure 5.** Snow thickness and density (contours) for R21 (**a**), R21_DRIFT (**b**), and R21_DRIFT21 (**c**) at the SHEBA tower during the November 1997–June 1998 period.

(e.g., Domine et al., 2018; Sturm et al., 2002, and references therein). Without the snowdrift parameterization activated, the snowpack is not compacted near the surface (Fig. 5a). Consequently, the P76 (not shown, similar to R21) and R21 simulations fail to represent the typical Arctic wind slab layer. Alternatively, the default ISBA-ES snowdrift parameterization (Brun et al., 1997) tends to increase the near-surface density (Fig. 5b). However, the maximum density in the Brun et al. (1997) snowdrift parameterization is $350\,\mathrm{g\,m^{-3}}$, which is lower than the mean density of the wind slab layers found during SHEBA in Sturm et al. (2002) ($403\,\mathrm{g\,m^{-3}}$). Therefore, the P76_DRIFT (not shown, similar to R21_DRFT) and R21_DRIFT simulations still lack an accurate representation of the wind slabs. In contrast, the Royer et al. (2021) snowdrift parameterization allows for higher densities and yields significantly different results (Fig. 5c). During winter, R21_DRIFT21 simulates higher densities near the snowpack surface, which could be attributed to a wind slab layer. Thus, although R21_DRIFT21 appears to overestimate the mean density, likely due to an inaccurate representation of the depth hoar layer, it does allow for a more realistic representation of wind slab layers in the Arctic region. In SI$^3$, the density is constant and equal to $330\,\mathrm{g\,m^{-3}}$. The snow mass (not shown) remains unaffected by the choice of the parameterization for snowfall density and/or wind-induced compaction in the accumulation period.

In the melt season, however, the melt rates are affected by the differences in heat diffusion associated with the differences in thermal conductivity, themselves dependent on the snow density.

Indeed, the snow density drives its thermal conductivity and thus the heat transfer within the snowpack. In SI$^3$, it is a fixed parameter at $0.31\,\mathrm{W\,m^{-1}\,K^{-1}}$ (Vancoppenolle et al., 2023), which is the value measured during SHEBA by Sturm et al. (2002), but in ISBA-ES it can evolve as a function of the density. Figure 6 represents the time series of the snow thermal conductivity for SI$^3$-only and SI$^3$+ISBAES simulations. The snowpack bulk conductivity from December 1997 to April 1998 is $0.10\,\mathrm{W\,m^{-1}\,K^{-1}}$ for the simulations without the snowdrift parameterization, $0.11\,\mathrm{W\,m^{-1}\,K^{-1}}$ for the simulations using the Brun et al. (1997) snowdrift parameterization, and $0.14\,\mathrm{W\,m^{-1}\,K^{-1}}$ with the Royer et al. (2021) snowdrift parameters. Those conductivity estimates are consistent with the measured bulk conductivity during SHEBA ($0.14\,\mathrm{W\,m^{-1}\,K^{-1}}$, Sturm et al., 2002) but since the publication of the SHEBA datasets the conductivity measurements have been questioned and they are thought to be too low (Calonne et al., 2019; Riche and Schneebeli, 2013). Sturm et al. (2002) estimated a thermal conductivity of $0.31\,\mathrm{W\,m^{-1}\,K^{-1}}$, inferred from ice growth and temperature gradients. Thus, the thermal conductivity simulated by ISBA-ES might be slightly underestimated.
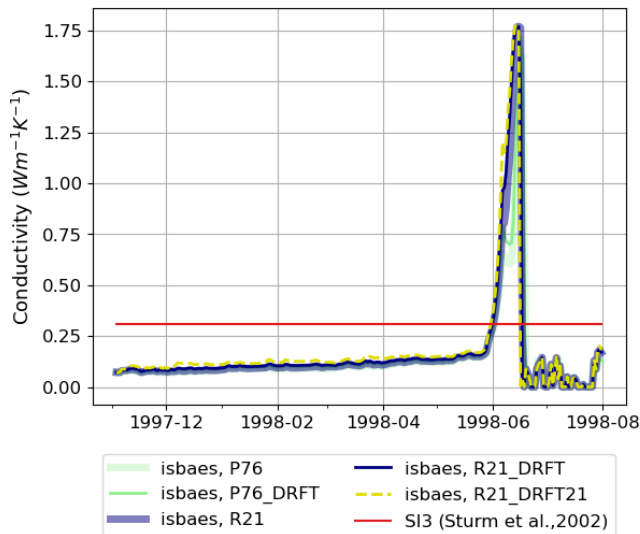
**Figure 6.** Snow conductivity at the SHEBA tower during the November 1997–September 1998 period.

The thermal conductivity drives the heat transfer through the snowpack. The snow surface temperature and the snow–ice interface temperature were measured at the SHEBA tower during the whole SHEBA period. Figure 7 represents the measured and simulated snow temperatures at both the snow surface and at the sea–ice interface. Note that the snow temperatures were not available in the SnowModel-LG outputs. The snow surface temperature is strongly dependent on the atmospheric forcing, and all $SI^3$ + ISBA-ES or $SI^3$-only simulations compare well with the observations and simulate a snow surface temperature consistent with the observations and a realistic temporal variability. The surface temperature simulated by ISBA-ES simulations is slightly too cold by between $\sim -3$ and $-4\,°C$ compared to the observations, while the bias in the $SI^3$-only simulation is about $-2.4\,°C$ on average over the accumulation and melt periods (from January to June 1998). All $SI^3$ + ISBA-ES simulations simulate a snow–ice interfacial temperature more consistent with the observations than the $SI^3$-only simulation, with a mean difference of $0.8\,°C$ for P76 and $-2.7\,°C$ for R21_DRFT21 simulations, against $-6\,°C$ for $SI^3$ on average over the accumulation and melt periods. Thus, this suggests that the thermal conductivity simulated by ISBA-ES is more realistic than the mean value used in $SI^3$ (even though it seems slightly underestimated compared to the observations). The ISBA-ES model also simulates a more realistic bottom snow temperature in the melt season (from the end of May) compared to $SI^3$. Note that the best agreement with the observations is found for the P76_DRIFT simulation. The lowest interfacial temperatures simulated by the $SI^3$ + ISBA-ES range from $\sim -12\,°C$ for P76 to $\sim -18\,°C$ for R21_DRIFT21 simulations. Note that this range depends on the parameterization used for the computation of the snow thermal conduc-

tivity (i.e., Sturm et al., 1997, parameterization), as we found a bigger range of temperatures with the Anderson (1976) parameterization (used in the ISBA-ES default version) (not shown). In brief, these results highlight the sensitivity of the snowpack bottom temperature to the choice of the parameterization for the snowfall density and/or wind compaction through their impact on the snow density and ultimately the snow conductivity, but also the importance of simulating a realistic thermal conductivity in the snowpack as it will condition the sea ice growth and melt below.

In all ISBA-ES simulations, the thermal conductivity of snow is lower than the value prescribed in $SI^3$. This results in a more insulating snow layer that reduces heat loss from the sea ice to the atmosphere, thereby keeping the ice warmer and thinner (Fig. 8). Consequently, all ISBA-ES simulations produce thinner sea ice compared to $SI^3$, with mean sea ice thicknesses (averaged from November 1997 to August 1998) of 2.17, 2.21, 2.18, 2.22, and 2.26 m for the P76, P76_DRFT, R21, R21_DRFT, and R21_DRFT21 experiments, respectively, versus 2.36 m in $SI^3$. While $SI^3$ simulates a mean sea ice thickness closer to the observed value of 2.38 m during the same period, the onset of melting is delayed by approximately 15 d relative to the observations. In contrast, although the ISBA-ES simulations underestimate the sea ice thickness, they reproduce a melt onset timing that aligns well with the observations. The sensitivity of the sea ice thickness to the choice of the parameterization for the snowfall density and the snowdrift is around 6 cm on average over the SHEBA period (R21_DRFT21-P76_DRFT). However, since the sea ice thickness at the end of the melt season is different between the different simulations, we could expect this sensitivity to grow in longer simulations.

The snow/ice albedo was also measured at the SHEBA tower during the melt season, and it is represented in Fig. 9 along with the albedo simulated by $SI^3$ + ISBA-ES and $SI^3$-only simulations. In $SI^3$, the snow albedo is fixed to 0.83 and it is constant during the accumulation period, which is roughly consistent with the observations at the SHEBA tower (Fig. 9). In $SI^3$ + ISBA-ES simulations, the albedo varies with the snowpack density and thus it is sensitive to the choice of the parameterization for the snowfall density and/or wind compaction. It is slightly lower than the albedo in $SI^3$ as it is bounded to 0.83 and decreases when the density increases. P76 and R21 simulate a realistic albedo, but the other simulations underestimate the albedo. When the snowdrift parameterization is active, the albedo fluctuates more as it depends on the density of the first layer, which is very sensitive to the compaction by wind.

## 4   Discussion and conclusion

Here we implemented for the first time a detailed snow-physics scheme (ISBA-ES) into a sea ice model ($SI^3$), which serves as the sea ice component for upcoming versions of
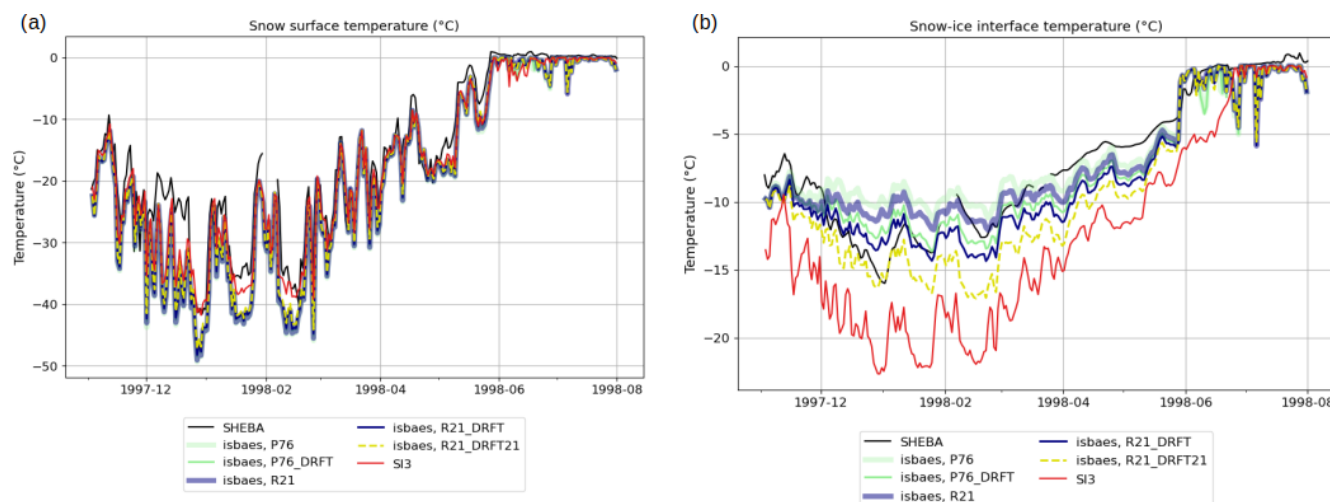
**Figure 7.** Measured and simulated snow surface **(a)** and snow–ice interface **(b)** temperatures (°C) at the SHEBA tower during the November 1997–September 1998 period. The black line shows the observations; the colored lines show the simulations as in Fig. 3.
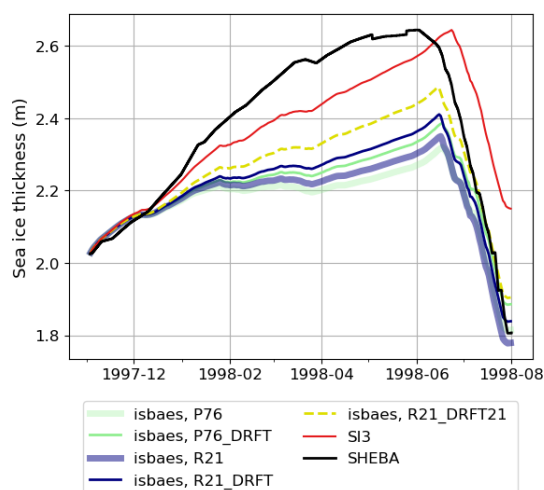


**Figure 8.** Measured and simulated sea ice thicknesses (m) at the SHEBA tower.

the CNRM-CM climate model. The ISBA-ES snow model incorporates detailed representations of snowpack properties such as density, grain size, and thermal conductivity, allowing for more accurate simulation of snow accumulation, compaction, metamorphism, and melt processes than usual slab models (such as the original snow parameterization in SI[3] that uses a constant density and thermal conductivity). Its integration into SI[3] does not use a coupler and the ISBA-ES code is compiled within the SI[3] framework.

The integration of such a detailed snow model within a sea ice model is, per se, a technical challenge. We integrated ISBA-ES to SI[3] so that snow thermodynamic processes are not computed anymore by SI[3] but by ISBA-ES. However, we aimed at modifying as little as possible the ISBA-ES model to facilitate the phasing with the future versions of the model. Thus, some sea-ice-related processes (thus not resolved by this alpine snow model) such as the snow–ice formation are still resolved within the sea ice model. At the snow–ice interface, transfer of heat from snow to ice is made through a heat conduction flux. The SI[3] + ISBA-ES model is currently fully functional in 1D without the sea ice dynamics activated and conserves the heat, mass, and salt.

The aim of this article was to present the first developments made to allow the integration of ISBA-ES into SI[3] and the performance of the model, focusing on the thermodynamic processes only. Here, we validated the SI[3] + ISBA-ES model over 1D configurations following the path of the Heat Budget of the Arctic Ocean (SHEBA) experiment (Perovich et al., 1999). We performed several simulations using different parameterizations for computing the snowfall density and the compaction by wind to illustrate the sensitivity of our model to these parameterizations. We compared these simulations with the SHEBA observations and with the SnowModel-LG outputs from Stroeve et al. (2020), which is, to date, the most sophisticated and validated snow-on-sea ice model available. Overall, our model simulates realistic snow thicknesses, densities, and temperatures compared to the SHEBA observations and SnowModel-LG outputs and captures the temporal variability of these variables well. Compared to the previous snow scheme used in SI[3] that assumes constant snow density and thermal conductivity, our model is able to realistically simulate the temporal evolution of the snow bulk density and thermal conductivity of the
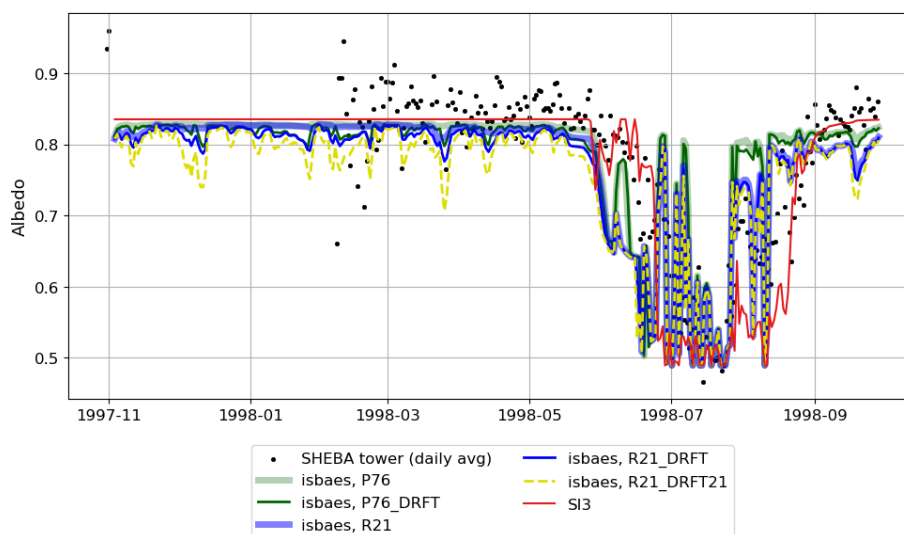
**Figure 9.** Daily averages of measured (dots) and simulated (lines) snow–ice albedo at the SHEBA tower during the November 1997–September 1998 period.

snowpack. As a result, the temperature at the snow–ice interface is more accurate with $SI^3$ +ISBAES compared to the previous $SI^3$ snow scheme, leading to a more realistic heat transfer to the underlying sea ice and more realistic sea ice upper temperatures. This emphasizes the importance of modeling the temporal changes in the density and thermal conductivity of the snow layers on Arctic sea ice. In ISBA-ES, the sea ice is more insulated from the atmosphere than in $SI^3$ due to the lower thermal conductivity of snow, which results in warmer and thinner ice. Consequently, the $SI^3$-only simulation yields a mean sea ice thickness closer to observations, whereas ISBA-ES appears to better capture the timing of the melt onset. This underestimation of sea ice thickness in the $SI^3$ + ISBA-ES simulations may result from several factors: (1) the one-dimensional nature of the simulation, which excludes dynamical processes; (2) the absence of certain physical processes, such as the formation of superimposed ice and the diffusion of water vapor through snow, that can influence sea ice growth; and (3) the $SI^3$ sea ice model being tuned for snow with higher thermal conductivity. Nonetheless, the results show a physically consistent response of sea ice thickness and demonstrate a realistic coupling between snow and sea ice.

In agreement with Lecomte et al. (2013), we demonstrated that snowpack thicknesses, densities, and thermal conductivities are equally sensitive to the parameterization choices for computing snowfall density and representing snow compaction by wind, as well as to the choice of atmospheric forcing. Therefore, specific tuning of these ISBA-ES parameterizations is as crucial as having realistic forcing to accurately represent the snowpack over the Arctic. The best agreement with the SHEBA observations for snow thickness and temperature is achieved using the Brun et al. (1997) parame-

ters for snowfall density and snow compaction (the default parameters of ISBA-ES). However, given (1) the significant spatial variability of Arctic snow cover, (2) the resolution disparity between model grid cell area estimates and point measurements during SHEBA, and (3) the uncertainties in observations, it is difficult to highlight the superiority of any $SI^3$ + ISBA-ES configuration over another. Nonetheless, our results highlight the realism of the $SI^3$ + ISBA-ES model and the importance of the choice of such parameterizations.

However, our study highlights the limitations of the current version of the $SI^3$ + ISBA-ES model. While the model produces realistic depth-averaged densities, the vertical density profiles it simulates are not accurate. The model fails to accurately represent the typical Arctic snowpack, which generally features a basal depth hoar layer beneath a hard, dense wind slab. This inaccurate representation of the density profiles suggests that certain polar-specific processes may be missing from the model. For instance, incorporating a representation of water vapor fluxes within the snowpack could benefit the model. Indeed, the strong temperature gradients in the Arctic snowpack create gradients in saturation water vapor density and pressure, which result in diffusion (Sturm and Benson, 1997) that can significantly influence the snowpack's density profiles (Domine et al., 2016; Jafari and Lehning, 2023). In addition, we also demonstrated that the default maximum density according to Brun et al. (1997) for the snowdrift parameterization is insufficient for accurately capturing the upper wind slab layer typical of the Arctic region. Setting a higher maximum density as proposed by Royer et al. (2021) appears to better represent this wind slab layer, although it results in a slightly overly dense snowpack. However, the absence of long-term records of snow density profiles over sea ice complicates the tuning of wind compaction

parameterizations. Future field studies collecting such data could significantly enhance the fidelity of density profiles in Arctic snow models. The model also seems to overestimate the albedo decrease during the melt season, leading to a rapid snowmelt. This underestimation is possibly due to a misrepresentation of the surface scattering layer in our model that was observed in the melt season during SHEBA (Perovich, 2005).

The model could also be further improved by incorporating specific snow-on-sea ice processes that are not yet represented in $SI^3$ + ISBA-ES, such as the formation of superimposed ice, or by incorporating more recent parameterizations of the thermal conductivity (e.g., Macfarlane et al., 2023). Thus, despite the current limitations of the model, the implementation of such an intermediate-complexity snow model within the $SI^3$ framework will facilitate further developments (in particular, the inclusion of polar-specific snow processes) that were not achievable with the previous, overly simplistic bulk snow model of $SI^3$.

Since this study focuses solely on the thermodynamics of snow and sea ice, it serves as a preliminary step towards the full integration of ISBA-ES within $SI^3$ and, subsequently, the CNRM-CM framework. The complete integration of ISBA-ES within $SI^3$ requires the implementation of advection for time-varying snow layers, which is currently in progress. The next version of the model will be capable of simulating the spatial and temporal evolution of the snowpack on both level and deformed ice, thanks to the use of multiple sea ice categories and the incorporation of a subgrid-scale distribution of snow thicknesses.

Following this, $SI^3$ + ISBA-ES must be coupled with the atmosphere to achieve its full integration within the CNRM-CM framework. This will require additional development to enable the snow model to be driven by atmospheric heat fluxes. In the current code version, these fluxes over snow are calculated within the ISBA-ES model, which is appropriate for a forced mode but not feasible within the existing CNRM-CM coupling approach, where surface heat fluxes are typically calculated in the atmospheric model. To conclude, this paper marks the starting point of developments towards an improved snow over sea ice in the CNRM-CM model.

*Author contributions.* TB: writing – review and editing, writing – original draft, visualization, validation, methodology, investigation, formal analysis, data curation, conceptualization. VG: writing – review and editing, supervision, methodology, funding acquisition, technical and scientific support. MV: writing – review and editing, technical and scientific support. CR: writing – review and editing, technical and scientific support. BD: writing – review and editing, technical and scientific support.

*Competing interests.* The contact author has declared that none of the authors has any competing interests.

*Disclaimer.* Publisher's note: Copernicus Publications remains neutral with regard to jurisdictional claims made in the text, published maps, institutional affiliations, or any other geographical representation in this paper. While Copernicus Publications makes every effort to include appropriate place names, the final responsibility lies with the authors.

*Review statement.* This paper was edited by Riccardo Farneti and reviewed by two anonymous referees.

# References

Anderson, E. A.: A Point Energy and Mass Balance Model of a Snow Cover, U.S. Department of Commerce, National Oceanic and Atmospheric Administration, National Weather Service, Office of Hydrology, 172 pp., 1976.

Bitz, C. M. and Lipscomb, W. H.: An energy-conserving thermodynamic model of sea ice, J. Geophys. Res.-Oceans, 104, 15669–15677, https://doi.org/10.1029/1999JC900100, 1999.

Bitz, C. M., Holland, M. M., Weaver, A. J., and Eby, M.: Simulating the ice-thickness distribution in a coupled climate model, J. Geophys. Res.-Oceans, 106, 2441–2463, https://doi.org/10.1029/1999JC000113, 2001.

Bohren, C. F. and Barkstrom, B. R.: Theory of the optical properties of snow, J. Geophys. Res., 79, 4527–4535, https://doi.org/10.1029/JC079i030p04527, 1974.

Bohren, C. F. and Beschta, R. L.: Snowpack albedo and snow density, Cold Reg. Sci. Technol., 1, 47–50, https://doi.org/10.1016/0165-232X(79)90018-1, 1979.

Boone, A.: Description du Schema de Neige ISBA-ES (Explicit Snow), 2002.

Boone, A. and Etchevers, P.: An Intercomparison of Three Snow Schemes of Varying Complexity Coupled to the Same Land Surface Model: Local-Scale Evaluation at an Alpine Site, J. Hydrometeor., 2, 374–394, https://doi.org/10.1175/1525-7541(2001)002<0374:AIOTSS>2.0.CO;2, 2001.

Brivoal, T.: NEMO_SI3_ISBAES_fortran_source_files_and_namelists, Zenodo [code], https://doi.org/10.5281/zenodo.14719233, 2024a.

Brivoal, T.: FORCINGS_SI3_ISBAES_SHEBA, Zenodo [data set], https://doi.org/10.5281/zenodo.14720364, 2024b.

Brivoal, T.: DATA_SI3_ISBAES_VALIDATION_AT_SHEBA, Zenodo [data set], https://doi.org/10.5281/zenodo.14720517, 2025.

Brun, E., Martin, E., Simon, V., Gendre, C., and Coleou, C.: An Energy and Mass Model of Snow Cover Suitable for Operational Avalanche Forecasting, J. Glaciol., 35, 333–342, https://doi.org/10.3189/S0022143000009254, 1989.

Brun, E., Martin, E., and Spiridonov, V.: Coupling a multi-layered snow model with a GCM, Ann. Glaciol., 25, 66–72, https://doi.org/10.3189/S0260305500013811, 1997.

Calonne, N., Milliancourt, L., Burr, A., Philip, A., Martin, C. L., Flin, F., and Geindreau, C.: Thermal Conductivity of Snow, Firn, and Porous Ice From 3-D Image-Based Computations, Geophys. Res. Lett., 46, 13079–13089, https://doi.org/10.1029/2019GL085228, 2019.

Decharme, B., Brun, E., Boone, A., Delire, C., Le Moigne, P., and Morin, S.: Impacts of snow and organic soils parameterization on northern Eurasian soil temperature profiles simulated by the ISBA land surface model, The Cryosphere, 10, 853–877, https://doi.org/10.5194/tc-10-853-2016, 2016.

Domine, F., Barrere, M., and Sarrazin, D.: Seasonal evolution of the effective thermal conductivity of the snow and the soil in high Arctic herb tundra at Bylot Island, Canada, The Cryosphere, 10, 2573–2588, https://doi.org/10.5194/tc-10-2573-2016, 2016.

Domine, F., Gauthier, G., Vionnet, V., Fauteux, D., Dumont, M., and Barrere, M.: Snow physical properties may be a significant determinant of lemming population dynamics in the high Arctic, Arct. Sci., 4, 813–826, https://doi.org/10.1139/as-2018-0008, 2018.

Douville, H.: La neige et sa paramétrisation dans les simulations climatiques, PhD thesis, Université Toulouse III, https://theses.fr/1995TOU30253 (last access: 30 September 2025), 1995.

Fichefet, T., Tartinville, B., and Goosse, H.: Sensitivity of the Antarctic sea ice to the thermal conductivity of snow, Geophys. Res. Lett., 27, 401–404, https://doi.org/10.1029/1999GL002397, 2000.

Gelaro, R., McCarty, W., Suárez, M. J., Todling, R., Molod, A., Takacs, L., Randles, C., Darmenov, A., Bosilovich, M. G., Reichle, R., Wargan, K., Coy, L., Cullather, R., Draper, C., Akella, S., Buchard, V., Conaty, A., da Silva, A., Gu, W., Kim, G.-K., Koster, R., Lucchesi, R., Merkova, D., Nielsen, J. E., Partyka, G., Pawson, S., Putman, W., Rienecker, M., Schubert, S. D., Sienkiewicz, M., and Zhao, B.: The Modern-Era Retrospective Analysis for Research and Applications, Version 2 (MERRA-2), J. Climate, 30, 5419–5454, https://doi.org/10.1175/JCLI-D-16-0758.1, 2017.

Gurvan, M., Bourdallé-Badie, R., Chanut, J., Clementi, E., Coward, A., Ethé, C., Iovino, D., Lea, D., Lévy, C., Lovato, T., Martin, N., Masson, S., Mocavero, S., Rousset, C., Storkey, D., Müeller, S., Nurser, G., Bell, M., Samson, G., Mathiot, P., Mele, F., and Moulin, A.: NEMO ocean engine, Zenodo [code], https://doi.org/10.5281/zenodo.6334656, 2022.

Hersbach, H., Bell, B., Berrisford, P., Hirahara, S., Horányi, A., Muñoz-Sabater, J., Nicolas, J., Peubey, C., Radu, R., Schepers, D., Simmons, A., Soci, C., Abdalla, S., Abellan, X., Balsamo, G., Bechtold, P., Biavati, G., Bidlot, J., Bonavita, M., De Chiara, G., Dahlgren, P., Dee, D., Diamantakis, M., Dragani, R., Flemming, J., Forbes, R., Fuentes, M., Geer, A., Haimberger, L., Healy, S., Hogan, R. J., Hólm, E., Janisková, M., Keeley, S., Laloyaux, P., Lopez, P., Lupu, C., Radnoti, G., de Rosnay, P., Rozum, I., Vamborg, F., Villaume, S., and Thépaut, J.-N.: The ERA5 global reanalysis, Q. J. R. Meteorol. Soc., 146, 1999–2049, https://doi.org/10.1002/qj.3803, 2020.

Holland, M. M., Clemens-Sewall, D., Landrum, L., Light, B., Perovich, D., Polashenski, C., Smith, M., and Webster, M.: The influence of snow on sea ice as assessed from simulations of CESM2, The Cryosphere, 15, 4981–4998, https://doi.org/10.5194/tc-15-4981-2021, 2021.

Hunke, E., Lipscomb, W., Jones, P., Turner, A., Jeffery, N., and Elliott, S.: CICE, The Los Alamos Sea Ice Model, Los Alamos National Laboratory (LANL), Los Alamos, NM (United States), 2017.

Itkin, P., Hendricks, S., Webster, M., von Albedyll, L., Arndt, S., Divine, D., Jaggi, M., Oggier, M., Raphael, I., Ricker, R., Rohde, J., Schneebeli, M., and Liston, G. E.: Sea ice and snow characteristics from year-long transects at the MOSAiC Central Observatory, Elem. Sci. Anthr., 11, 00048, https://doi.org/10.1525/elementa.2022.00048, 2023.

Jafari, M. and Lehning, M.: Convection of snow: when and why does it happen?, Front. Earth Sci., 11, https://doi.org/10.3389/feart.2023.1167760, 2023.

Jutras, M., Vancoppenolle, M., Lourenço, A., Vivier, F., Carnat, G., Madec, G., Rousset, C., and Tison, J.-L.: Thermodynamics of slush and snow–ice formation in the Antarctic sea-ice zone, Deep Sea Res. Part II Top. Stud. Oceanogr., 131, 75–83, https://doi.org/10.1016/j.dsr2.2016.03.008, 2016.

Kojima, K.: Densification of Seasonal Snow Cover, Phys. Snow Ice Proc., 1, 929–952, 1967.

Kondo, J. and Yamazaki, T.: A Prediction Model for Snowmelt, Snow Surface Temperature and Freezing Depth Using a Heat Balance Method, Appl. Meteor. Climatol., 29, 375–384, https://doi.org/10.1175/1520-0450(1990)029<0375:APMFSS>2.0.CO;2, 1990.

Large, W. and Yeager, S.: Diurnal to decadal global forcing for ocean and sea-ice models: The data sets and flux climatologies, UCAR/NCAR, https://doi.org/10.5065/D6KK98Q6, 2004.

Lecomte, O., Fichefet, T., Vancoppenolle, M., Domine, F., Massonnet, F., Mathiot, P., Morin, S., and Barriat, P. y.: On the formulation of snow thermal conductivity in large-scale sea ice models, J. Adv. Model. Earth Syst., 5, 542–557, https://doi.org/10.1002/jame.20039, 2013.

Lellouche, J.-M., Greiner, E., Le Galloudec, O., Garric, G., Regnier, C., Drevillon, M., Benkiran, M., Testut, C.-E., Bourdalle-Badie, R., Gasparin, F., Hernandez, O., Levier, B., Drillet, Y., Remy, E., and Le Traon, P.-Y.: Recent updates to the Copernicus Marine Service global ocean monitoring and forecasting real-time 1/12° high-resolution system, Ocean Sci., 14, 1093–1126, https://doi.org/10.5194/os-14-1093-2018, 2018.

Leonard, K. C. and Maksym, T.: The importance of wind-blown snow redistribution to snow accumulation on Bellingshausen Sea ice, Ann. Glaciol., 52, 271–278, https://doi.org/10.3189/172756411795931651, 2011.

Liston, G. E., Itkin, P., Stroeve, J., Tschudi, M., Stewart, J. S., Pedersen, S. H., Reinking, A. K., and Elder, K.: A Lagrangian Snow-Evolution System for Sea-Ice Applications (SnowModel-LG): Part I—Model Description, J. Geophys. Res.-Oceans, 125, e2019JC015913, https://doi.org/10.1029/2019JC015913, 2020.

Liston, G. E., Stroeve, J., and Itkin, P.: Lagrangian Snow Distributions for Sea-Ice Applications, Version 1, Boulder, Colorado USA, NASA National Snow and Ice Data Center Distributed Active Archive Center [data set], https://doi.org/10.5067/27A0P5M6LZBI, 2021.

Loth, B., Graf, H.-F., and Oberhuber, J. M.: Snow cover model for global climate simulations, J. Geophys. Res.-Atmos., 98, 10451–10464, https://doi.org/10.1029/93JD00324, 1993.

Lynch-Stieglitz, M.: The Development and Validation of a Simple Snow Model for the GISS GCM, https://doi.org/10.1175/1520-0442(1994)007<1842:TDAVOA>2.0.CO;2, 1994.

Macfarlane, A. R., Löwe, H., Gimenes, L., Wagner, D. N., Dadic, R., Ottersberg, R., Hämmerle, S., and Schneebeli, M.: Temporospatial variability of snow's thermal conductivity on Arctic sea ice, The Cryosphere, 17, 5417–5434, https://doi.org/10.5194/tc-17-5417-2023, 2023.

Madec, G. and the NEMO System Team: NEMO Ocean Engine Reference Manual, Zenodo, https://doi.org/10.5281/zenodo.1464816, 2024.

Mellor, M.: Properties of snow, https://erdc-library.erdc.dren.mil/items/81b728f7-5e0b-4ef8-e053-411ac80adeb3 (last access: 29 September 2025), 1964.

Nicolaus, M., Haas, C., and Bareiss, J.: Observations of superimposed ice formation at melt-onset on fast ice on Kongsfjorden, Svalbard, Phys. Chem. Earth Parts ABC, 28, 1241–1248, https://doi.org/10.1016/j.pce.2003.08.048, 2003.

Nicolaus, M., Perovich, D. K., Spreen, G., Granskog, M. A., von Albedyll, L., Angelopoulos, M., Anhaus, P., Arndt, S., Belter, H. J., Bessonov, V., Birnbaum, G., Brauchle, J., Calmer, R., Cardellach, E., Cheng, B., Clemens-Sewall, D., Dadic, R., Damm, E., de Boer, G., Demir, O., Dethloff, K., Divine, D. V., Fong, A. A., Fons, S., Frey, M. M., Fuchs, N., Gabarró, C., Gerland, S., Goessling, H. F., Gradinger, R., Haapala, J., Haas, C., Hamilton, J., Hannula, H.-R., Hendricks, S., Herber, A., Heuzé, C., Hoppmann, M., Høyland, K. V., Huntemann, M., Hutchings, J. K., Hwang, B., Itkin, P., Jacobi, H.-W., Jaggi, M., Jutila, A., Kaleschke, L., Katlein, C., Kolabutin, N., Krampe, D., Kristensen, S. S., Krumpen, T., Kurtz, N., Lampert, A., Lange, B. A., Lei, R., Light, B., Linhardt, F., Liston, G. E., Loose, B., Macfarlane, A. R., Mahmud, M., Matero, I. O., Maus, S., Morgenstern, A., Naderpour, R., Nandan, V., Niubom, A., Oggier, M., Oppelt, N., Pätzold, F., Perron, C., Petrovsky, T., Pirazzini, R., Polashenski, C., Rabe, B., Raphael, I. A., Regnery, J., Rex, M., Ricker, R., Riemann-Campe, K., Rinke, A., Rohde, J., Salganik, E., Scharien, R. K., Schiller, M., Schneebeli, M., Semmling, M., Shimanchuk, E., Shupe, M. D., Smith, M. M., Smolyanitsky, V., Sokolov, V., Stanton, T., Stroeve, J., Thielke, L., Timofeeva, A., Tonboe, R. T., Tavri, A., Tsamados, M., Wagner, D. N., Watkins, D., Webster, M., and Wendisch, M.: Overview of the MOSAiC expedition: Snow and sea ice, Elem. Sci. Anthr., 10, 000046, https://doi.org/10.1525/elementa.2021.000046, 2022.

Pahaut, E.: Les cristaux de neige et leurs métamorphoses (), Centre d'Étude de la Neige, 58 pp., 1975.

Perovich, D. K.: On the aggregate-scale partitioning of solar radiation in Arctic sea ice during the Surface Heat Budget of the Arctic Ocean (SHEBA) field experiment, J. Geophys. Res.-Oceans, 110, https://doi.org/10.1029/2004JC002512, 2005.

Perovich, D. K. and Polashenski, C.: Albedo evolution of seasonal Arctic sea ice, Geophys. Res. Lett., 39, https://doi.org/10.1029/2012GL051432, 2012.

Perovich, D. K., Grenfell, T. C., Light, B., Richter-Menge, J. A., Sturm, M., Tucker III, W. B., Eicken, H., Maykut, G. A., and Elder, B.: SHEBA: Snow and Ice Studies CD-ROM, https://psl.noaa.gov/arctic/sheba/netcdf/datasets/Ice_snow_data/ICEWEB/INDEX.HTM (last access: 29 September 2025), 1999.

Persson, P. O. G., Fairall, C. W., Andreas, E. L., Guest, P. S., and Perovich, D. K.: Measurements near the Atmospheric Surface Flux Group tower at SHEBA: Near-surface conditions and surface energy budget, J. Geophys. Res.-Oceans, 107, SHE 21-1–SHE 21-35, https://doi.org/10.1029/2000JC000705, 2002.

Petty, A. A., Webster, M., Boisvert, L., and Markus, T.: The NASA Eulerian Snow on Sea Ice Model (NESOSIM) v1.0: initial model development and analysis, Geosci. Model Dev., 11, 4577–4602, https://doi.org/10.5194/gmd-11-4577-2018, 2018.

Riche, F. and Schneebeli, M.: Thermal conductivity of snow measured by three independent methods and anisotropy considera-

tions, The Cryosphere, 7, 217–227, https://doi.org/10.5194/tc-7-217-2013, 2013.

Rousset, C., Vancoppenolle, M., Madec, G., Fichefet, T., Flavoni, S., Barthélemy, A., Benshila, R., Chanut, J., Levy, C., Masson, S., and Vivier, F.: The Louvain-La-Neuve sea ice model LIM3.6: global and regional capabilities, Geosci. Model Dev., 8, 2991–3005, https://doi.org/10.5194/gmd-8-2991-2015, 2015.

Royer, A., Picard, G., Vargel, C., Langlois, A., Gouttevin, I., and Dumont, M.: Improved Simulation of Arctic Circumpolar Land Area Snow Properties and Soil Temperatures, Front. Earth Sci., 9, https://doi.org/10.3389/feart.2021.685140, 2021.

Shapero, D. R., Badgeley, J. A., Hoffman, A. O., and Joughin, I. R.: icepack: a new glacier flow modeling package in Python, version 1.0, Geosci. Model Dev., 14, 4593–4616, https://doi.org/10.5194/gmd-14-4593-2021, 2021.

Sommer, C. G., Lehning, M., and Fierz, C.: Wind Tunnel Experiments: Influence of Erosion and Deposition on Wind-Packing of New Snow, Front. Earth Sci., 6, https://doi.org/10.3389/feart.2018.00004, 2018.

Stroeve, J., Liston, G. E., Buzzard, S., Zhou, L., Mallett, R., Barrett, A., Tschudi, M., Tsamados, M., Itkin, P., and Stewart, J. S.: A Lagrangian Snow Evolution System for Sea Ice Applications (SnowModel-LG): Part II—Analyses, J. Geophys. Res.-Oceans, 125, e2019JC015900, https://doi.org/10.1029/2019JC015900, 2020.

Sturm, M. and Benson, C. S.: Vapor transport, grain growth and depth-hoar development in the subarctic snow, J. Glaciol., 43, 42–59, https://doi.org/10.3189/S0022143000002793, 1997.

Sturm, M. and Massom, R. A.: Snow in the sea ice system: friend or foe?, in: Sea Ice, John Wiley & Sons, Ltd, 65–109, https://doi.org/10.1002/9781118778371.ch3, 2017.

Sturm, M., Holmgren, J., König, M., and Morris, K.: The thermal conductivity of seasonal snow, J. Glaciol., 43, 26–41, https://doi.org/10.3189/S0022143000002781, 1997.

Sturm, M., Holmgren, J., and Perovich, D. K.: Winter snow cover on the sea ice of the Arctic Ocean at the Surface Heat Budget of the Arctic Ocean (SHEBA): Temporal evolution and spatial variability, J. Geophys. Res.-Oceans, 107, SHE 23-1–SHE 23-17, https://doi.org/10.1029/2000JC000400, 2002.

Sun, S., Jin, J., and Xue, Y.: A simple snow-atmosphere-soil transfer model, J. Geophys. Res.-Atmos., 104, 19587–19597, https://doi.org/10.1029/1999JD900305, 1999.

Thorndike, A. S., Rothrock, D. A., Maykut, G. A., and Colony, R.: The thickness distribution of sea ice, J. Geophys. Res., 80, 4501–4513, https://doi.org/10.1029/JC080i033p04501, 1975.

Vancoppenolle, M., Fichefet, T., Goosse, H., Bouillon, S., Madec, G., and Maqueda, M. A. M.: Simulating the mass balance and salinity of Arctic and Antarctic sea ice. 1. Model description and validation, Ocean Model., 27, 33–53, https://doi.org/10.1016/j.ocemod.2008.10.005, 2009.

Vancoppenolle, M., Rousset, C., Blockley, E., Aksenov, Y., Feltham, D., Fichefet, T., Garric, G., Guémas, V., Iovino, D., Keeley, S., Madec, G., Massonnet, F., Ridley, J., Schroeder, D., and Tietsche, S.: SI3, the NEMO Sea Ice Engine, Zenodo [code], https://doi.org/10.5281/zenodo.7534900, 2023.

Verseghy, D. L.: Class-A Canadian land surface scheme for GCMS. I. Soil model, Int. J. Climatol., 11, 111–133, https://doi.org/10.1002/joc.3370110202, 1991.

Vionnet, V., Brun, E., Morin, S., Boone, A., Faroux, S., Le Moigne, P., Martin, E., and Willemet, J.-M.: The detailed snowpack scheme Crocus and its implementation in SURFEX v7.2, Geosci. Model Dev., 5, 773–791, https://doi.org/10.5194/gmd-5-773-2012, 2012.

Voldoire, A., Sanchez-Gomez, E., Salas y Mélia, D., Decharme, B., Cassou, C., Sénési, S., Valcke, S., Beau, I., Alias, A., Chevallier, M., Déqué, M., Deshayes, J., Douville, H., Fernandez, E., Madec, G., Maisonnave, E., Moine, M.-P., Planton, S., Saint-Martin, D., Szopa, S., Tyteca, S., Alkama, R., Belamari, S., Braun, A., Coquart, L., and Chauvin, F.: The CNRM-CM5.1 global climate model: description and basic evaluation, Clim. Dynam., 40, 2091–2121, https://doi.org/10.1007/s00382-011-1259-y, 2013.

Wagner, D. N., Shupe, M. D., Cox, C., Persson, O. G., Uttal, T., Frey, M. M., Kirchgaessner, A., Schneebeli, M., Jaggi, M., Macfarlane, A. R., Itkin, P., Arndt, S., Hendricks, S., Krampe, D., Nicolaus, M., Ricker, R., Regnery, J., Kolabutin, N., Shimanshuck, E., Oggier, M., Raphael, I., Stroeve, J., and Lehning, M.: Snowfall and snow accumulation during the MOSAiC winter and spring seasons, The Cryosphere, 16, 2373–2402, https://doi.org/10.5194/tc-16-2373-2022, 2022.

Webster, M., Gerland, S., Holland, M., Hunke, E., Kwok, R., Lecomte, O., Massom, R., Perovich, D., and Sturm, M.: Snow in the changing sea-ice systems, Nat. Clim. Change, 8, 946–953, https://doi.org/10.1038/s41558-018-0286-7, 2018.

Wever, N., Rossmann, L., Maaß, N., Leonard, K. C., Kaleschke, L., Nicolaus, M., and Lehning, M.: Version 1 of a sea ice module for the physics-based, detailed, multi-layer SNOWPACK model, Geosci. Model Dev., 13, 99–119, https://doi.org/10.5194/gmd-13-99-2020, 2020.

Xiong, C. and Shi, J.: Snow specific surface area remote sensing retrieval using a microstructure based reflectance model, Remote Sens. Environ., 204, 838–849, https://doi.org/10.1016/j.rse.2017.09.017, 2018.